

# Machine Learning for Stretchable Organic Integrated Circuit Design

Luke Qiao, Xingyu (Brian) Zhou, Adhavan Jayabalan

Stanford University

lkqiao@stanford.edu, xzhou25@stanford.edu, addyj@stanford.edu

**Abstract**—We use machine learning (ML) to accelerate the design of stretchable organic neuromorphic integrated circuits fabricated with organic field-effect transistors (OFETs). Specifically, we study a mechanoreceptor pressure sensor whose output spike train encodes applied pressure in its firing frequency and pulse width. Directly searching the high-dimensional design space via circuit simulation is computationally expensive and requires greater intuition. To address this, we construct a dataset of 16,120 simulated circuits by sweeping circuit design parameters (CDPs) across different pressure levels in Cadence and recording the circuit output: minimum and maximum output frequency, average pulse width, average spike amplitude. We then develop a two-stage pipeline for inverse design. Stage 1 uses Bayesian Optimization (BO) to search for CDPs that best produce the desired output signal characteristics (OSCs), given a trained neural network (NN). Stage 2 is a generalized discriminant analysis (GDA) classifier that checks the validity of the proposed CDPs from the BO algorithm. This framework enables data-driven, performance-directed design of emerging stretchable OFET design spaces.

## I. INTRODUCTION

### 1.1 Motivation

In analog integrated circuit (IC) design, we often face the task of finding the best CDPs given a set of output characteristics, e.g., total power consumption, maximum gain, signal-to-noise ratio, and maximum frequency. There exist protocols to find the best parameters, but they mostly apply to classic ICs fabricated with a standard silicon process, such as operational amplifiers. For non-conventional ICs fabricated in non-standard processes, e.g. stretchable organic neuromorphic ICs, finding the best parameters often requires trial and error. Thus, we aim to design a ML pipeline that is capable of inferring the best combinations of CDPs from a given set of OSCs for stretchable organic neuromorphic ICs. This would greatly streamline the process of optimizing the designs of such circuits.

### 1.2 Background and Overview

We focus our scope of study on a particular neuromorphic pressure mechanoreceptor circuit, fabricated with organic field-effect transistors (OFET). This circuit senses the applied pressure and outputs a spike train in  $I_{\text{out}}$  that encodes the magnitude of the pressure in its frequency. Considering this circuit as a single unit, multiple units can be arranged into a touch sensing array as an “electronic skin”. Due to limitations of the fabrication process for organic stretchable integrated circuits, multiple units must share a single output node. In

order to distinguish the output of one unit from another, the output spike train of each unit has its distinct pulse width. In this way, even if the outputs are summed, they can easily be decoupled. More details of the schematic and mechanism of operation of the mechanoreceptor circuit are explained in Appendix A.

The input to our proposed ML pipeline is a target vector that represents the desired OSCs of the circuit. The output of the pipeline is a predicted set of CDPs for the neuromorphic IC that will best achieve the desired OSCs.

## II. RELATED WORKS

### 2.1 Stretchable Integrated Circuits

Recent innovations in organic semiconducting materials have enabled the fabrication of intrinsically stretchable transistor devices [1], [2]. The inherent stretchability and functional versatility of these devices make them well-suited for applications such as sensory feedback in neuroprostheses and embodied intelligence. Previous work has demonstrated the integration of these electronic skins into the sensory-motor loop within animal models [3].

### 2.2 Neuromorphic Circuits and Sensors

Neuromorphic circuits emulate biological neurons by replicating their spiking voltage outputs in response to synaptic current injections [4]. Their inherent analog nature allows for highly diverse information encoding and processing with significantly reduced power consumption. While early neuromorphic IC research primarily focused on computation, recent works are increasingly exploring the integration of neuromorphic architectures into sensors for power-efficient on-edge processing and learning [5], [6]. However, the vast majority of research in neuromorphic ICs has been conducted using silicon-based circuits, with limited investigation into neuromorphic circuits implemented on intrinsically stretchable devices.

### 2.3 Machine Learning in Analog IC Design Optimization

Conventionally, analog IC design has been a manual, iterative process, heavily dependent on the expertise of circuit designers. Recent advancements in machine learning, utilizing reinforcement learning with circuit simulators [7], [8], are beginning to automate this process. While these systems can achieve designs surpassing human capabilities without

relying on extensive parameter sweeps, they are largely focused on traditional analog circuits like amplifiers and filters, often using established simulators and process design kits for silicon-based ICs. Although there exist ways to characterize single stretchable organic transistors [9], [10], the absence of complete process design kits for organic stretchable ICs significantly limits the feasibility of adapting these existing state-of-the-art ML strategies to optimize neuromorphic ICs implemented in the stretchable organic process.

### III. DATASET AND FEATURES

We generated a custom dataset with 16,120 datapoints. Each example  $(x, y)$  consists of the CDPs ( $x \in \mathbb{R}^5$ ) and their corresponding OSCs ( $y \in \mathbb{R}^4$ ).

The five CDPs are: 1) The capacitance of the feedback capacitor  $C_{fb}$ , parameterized by  $C_{fb}$ ; 2) The dimensions of OFETs  $M_4$  to  $M_7$ , parameterized by  $axInv\_L$ ; 3) The dimensions of OFET  $M_{rst}$ , parameterized by  $axRst\_L$ ; 4) The dimensions of the output OFET  $M_{out}$ , parameterized by  $out\_L$ ; and 5) The dimensions of the pressure sensing OFET  $M_{sens}$ , parameterized by  $sens\_L$ .

The four OSCs are: 1) The output frequency at lowest applied pressure, represented by  $f_{min}$ ; 2) The output frequency at highest applied pressure, represented by  $f_{max}$ ; 3) The average pulse width, represented by  $\tau$ ; and 4) The average spike amplitude, represented by  $a$ .

To characterize the behavior of the mechanoreceptor circuit, we ran a total of 92,928 simulations in Cadence Virtuoso ADE, sweeping a total of 6 parameters. Among these are 5 CDPs of the circuit, and the remaining parameter reflects the pressure applied to the circuit. It is assumed that the applied pressure would cause a change in the gate dielectric capacitance of  $M_{sens}$ , represented by  $C_{sens}$ . Therefore, each combination of  $(C_{fb}, axInv\_L, axRst\_L, out\_L, sens\_L)$  are simulated, 4 values of  $C_{sens}$  are simulated, in order to test the circuit's response to a varying range of applied pressure. That is, a total of  $92,928/4 = 23,232$  parameter combinations are simulated. More details of which values are chosen for each parameter are in Appendix B.

This simulated data allows us to analyze whether a CDP combination allows the circuit to produce spike trains in  $I_{out}$  at varying levels of applied pressure, and if so, at what frequencies, pulse widths and amplitudes. For our circuit design, we would like to ensure maximum sensitivity and widest possible operational pressure range. A CDP combination is considered “valid” if the output for all levels of simulated applied pressure is a spike train. If for any applied pressure the output is a flat line, the combination is considered “invalid.” As such, we add a label parameter `is_valid` to the dataset.

The frequency, pulse width and amplitude of the 92,928  $I_{out}$  current traces were extracted, and were used to determine whether a CDP combination is valid or not. Of the 23,232 CDP combinations, we found that 8,947 are valid. To balance the number of valid samples, we included a total of 7,173 invalid samples. Specifically, these invalid samples are chosen to be the least sensitive circuits, i.e. they do not produce spikes until

the simulated applied pressure reaches the highest level. The reason why this is done instead of simply randomly drawing from all invalid samples is elaborated in Appendix C.

Finally, because the features and labels spanned many orders of magnitude from  $10^{-10}$  to  $10^1$ , we standardized the values to follow the standard normal distribution  $\mathcal{N}(0, 1)$  for numerical stability and to improve model performances.

## IV. METHODS

We aim to identify CDPs that achieve a desired set of OSCs. Let the CDPs be denoted by  $x = (C_{fb}, axInv\_L, axRst\_L, out\_L, sens\_L)$  and the corresponding OSCs by  $y = (f_{min}, f_{max}, \tau, a)$ . Then, our goal is to solve design problem: given a desired target OSCs  $y_{target}$ , find CDPs  $x^*$  that produce similar behavior.

To address this inverse problem, we develop a two-stage pipeline as shown in Figure 1:

- **Stage 1 (CDPs Predictor).** We train a NN  $h_\theta : x \rightarrow y$  to approximate the Cadence simulator mapping from CDPs to OSCs. The model predicts  $\hat{y} = h_\theta(x) = (\hat{f}_{min}, \hat{f}_{max}, \hat{\tau}, \hat{a})$  for a given CDPs  $x$ . Once trained, we use BO to search over the space for CDPs  $x^*$  that minimize the discrepancy between the predicted OSCs and a desired target OSCs  $y_{target}$ .
- **Stage 2 (Verifier Model).** Not all generated CDPs correspond to valid circuits. To filter out invalid CDPs, we train a classifier  $g_\beta : x \rightarrow [0, 1]$ . The classifier is trained using the binary `is_valid` flag from the dataset. At inference time, we use  $g_\beta(x)$  to discard the invalid proposed design  $x^*$  produced by the BO procedure, improving the quality and robustness of the final CDPs.

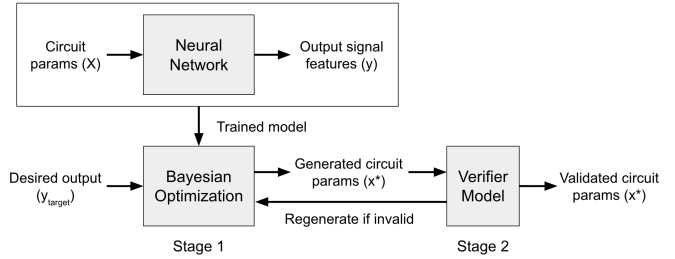


Fig. 1. Two-stage model pipeline

### 4.1 Stage 1 Algorithms

**Fully Connected Neural Network:** We use a fully connected feedforward NN to define the mapping  $h_\theta : x \rightarrow y$ . The input  $x \in \mathbb{R}^5$  corresponds to the CDPs ( $C_{fb}, axInv\_L, axRst\_L, out\_L, sens\_L$ ), and the output  $\hat{y} \in \mathbb{R}^4$  corresponds to the predicted OSCs ( $\hat{f}_{min}, \hat{f}_{max}, \hat{\tau}, \hat{a}$ ). We formulate the NN as

$$\begin{aligned} z^{(0)} &= x \\ z^{(\ell)} &= \sigma(W^{(\ell)}z^{(\ell-1)} + b^{(\ell)}), \quad \ell = 1, 2, 3 \\ \hat{y} &= h_\theta(x) = W^{(4)}z^{(3)} + b^{(4)}, \end{aligned}$$

where  $\ell$  is the number of hidden layers,  $W^{(\ell)}$  and  $b^{(\ell)}$  are the weight matrices and bias vectors, and  $\sigma(u) = \max(0, u)$  is the ReLU activation function.

Given  $N$  training examples  $\{(x^{(i)}, y^{(i)})\}_{i=1}^N$ , we train the network as a multi-output regression model by minimizing the mean squared error (MSE) loss with  $\ell_2$  regularization:  $\mathcal{L}(\theta) = \frac{1}{N} \sum_{i=1}^N \|h_\theta(x^{(i)}) - y^{(i)}\|_2^2 + \lambda \|\theta\|_2^2$ , where  $\lambda$  is the regularization coefficient.

*Bayesian Optimization:* To generate CDPs  $x^*$  that most closely produce the desired target OSCs  $y_{\text{target}}$ , we use BO. Conceptually, BO searches over the design space of  $x$  by iteratively proposing updated predictions to minimize a certain objective function. We formulate the BO objective as

$$f(x) = \|\hat{y}(x) - y_{\text{target}}\|_2^2 + \lambda_{\text{manifold}} \min_i \|x - x_i^{\text{train}}\|_2^2,$$

where  $\hat{y}(x)$  denotes the trained NN predictions, and  $\lambda_{\text{manifold}}$  encourages the search to remain close to regions supported by the training data. In practice, we model  $f(x)$  with a Gaussian Process (GP) surrogate with the Matern kernel  $K(x, z) = \sigma_0^2 \text{Matern}_{\nu=2.5}(x, z) + \sigma_n^2 \delta_{x,z}$ , a popular choice for BO [11], where we have that

$$\text{Matern}_\nu(d) = \frac{2^{1-\nu}}{\Gamma(\nu)} \left( \frac{\sqrt{2\nu}d}{\ell} \right)^\nu K_\nu \left( \frac{\sqrt{2\nu}d}{\ell} \right),$$

with  $d = \|x - z\|$  and  $K_\nu$  being the Bessel function of the second kind.

At the  $t$ -th step, given observations  $\mathcal{D}_t = \{(x_j, f(x_j))\}_{j=1}^t$ , we fit the GP posterior mean and variance

$$\begin{aligned} \mu_t(x) &= K(x, X_t) K_t^{-1} f_t, \\ \sigma_t^2(x) &= K(x, x) - K(x, X_t) K_t^{-1} K(X_t, x), \end{aligned}$$

where  $K_{ij} = K(x_i, x_j)$ .

To propose new points  $x_{t+1}$ , we use the Expected Improvement (EI) acquisition function  $\text{EI}_t(x) = (f^* - \mu_t(x) - \xi) \Phi(Z) + \sigma_t(x) \phi(Z)$ , where  $Z = \frac{f^* - \mu_t(x) - \xi}{\sigma_t(x)}$  and  $\Phi$  and  $\phi$  are the CDF and PDF of the standard normal distribution, respectively. We generate candidate points from a trust region  $\{x^{(k)}\} \in \mathcal{T}_t$  around the current best point  $x_t^*$  via Sobol sequences for space-filling sampling [12]. The bounds in this trust region enforce realistic CDPs in the generated design. Then, we pick the next point  $x_{t+1}$  out of the candidates that maximizes  $\text{EI}_t(x)$ . This selected point is then evaluated with the true objective  $f(x_{t+1})$ , added to  $\mathcal{D}_{t+1}$ , and incorporated into the GP model. This process continues until the maximum number of iterations is reached, at which point the algorithm returns the proposed CDPs  $x^*$ .

#### 4.2 Stage 2 Algorithms

*GDA Classifier:* We trained a kernel-trick GDA classifier  $g_\beta : x \rightarrow [0, 1]$  to verify that the proposed CDPs  $x^*$  produced valid outputs, where 1 and 0 represent a valid and invalid circuit, respectively. We used the Gaussian, or Radial Basis Function (RBF), kernel  $K(x, z) := \exp(-\gamma \|x - z\|^2)$  to capture potential nonlinearities. Furthermore, we optimized the

model parameters using gradient descent with a least-mean-squares (LMS) loss function  $J(\beta) = \frac{1}{2N} \|y_i - (K\beta)_i\|_2^2$ .

During training, we update the model parameters  $\beta$  according to the rule  $\beta := \beta + \alpha(y - K\beta)$ . During inference, we compute  $h(x) = \sum_{i=1}^n \beta_i K(x^{(i)}, x)$  and assign  $g_\beta(x) = 1$  if  $h(x) > 0.5$  and  $g_\beta(x) = 0$  otherwise.

## V. EXPERIMENTS AND RESULTS

We trained and evaluated the NN and GDA models, and performed a model comparison study between the 1-Nearest Neighbor (1-NN) model baseline and our two-stage pipeline. Note that all models were trained on the same 70-15-15 training-test-validation split to avoid unintentional data leakage.

### 5.1 Fully Connected Neural Network

The fully connected NN has 3 hidden layers, each of width 64, with ReLU activation functions. In our implementation, we use the PyTorch `MSELoss` criterion and the Adam optimizer with learning rate  $\alpha = 10^{-3}$  and weight decay  $\lambda = 10^{-5}$  [13]. We train with mini-batches of size 64 for up to 200 epochs on CPU. We use early stopping based on the validation loss: whenever the validation loss decreases by at least  $10^{-4}$ , we save the current model parameters as the best-performing checkpoint, and we stop training if the validation loss does not improve for 20 consecutive epochs. After training, we reload the best-performing checkpoint for evaluation.

For evaluation, we compute the root mean squared error (RMSE) and coefficient of determination  $R^2$  for each output dimension in physical units. We collect the normalized predictions  $\hat{y}$  and targets  $y$ , apply the inverse normalization transform to recover physical quantities, and then compute RMSE and  $R^2$  using standard regression metrics. These metrics summarize how accurately the learned model  $h_\theta$  reproduces the simulator outputs across the validation and test sets. With the final set of hyperparameters, the model achieved RMSEs of 0.046 Hz for Min Frequency, 0.157 Hz for Max Frequency, 0.013 ms for Avg Pulse Width, and 0.009  $\mu\text{A}$  for Avg Spike Amplitude. The corresponding training and validation loss curves in Figure 2 show that the losses converge quickly and remain low, suggesting that the model is not overfitting.

To select model hyperparameters such as the number of hidden layers, width, and learning rate, we performed a small grid search. We trained networks with 2, 3, 4, and 5 hidden layers and different widths, and compared them using validation RMSE and  $R^2$  on the denormalized outputs. All of these architectures achieved very similar performance, indicating that model accuracy is not highly sensitive to depth or width in this range. We therefore chose 3 hidden layers with width 64 as a good trade-off between expressiveness, model complexity, and minimizing the risk of overfitting.

We also experimented with learning rates  $\alpha = 10^{-2}, 10^{-3}, 10^{-4}$ , and  $10^{-5}$  for the Adam optimizer under the same training protocol. A learning rate of  $10^{-2}$  produced noisy and unstable training and validation loss curves. In contrast,

learning rates between  $10^{-3}$  and  $10^{-5}$  yielded smooth monotonic decreases of both training and validation loss; smaller learning rates required substantially more epochs and did not lead to significant gains in validation RMSE or  $R^2$ . Based on this trade-off between stability and training time, we set the learning rate to  $10^{-3}$  for all subsequent experiments.

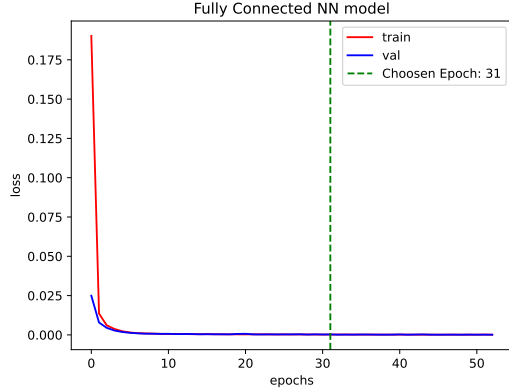


Fig. 2. Fully connected NN loss curve

## 5.2 GDA Classifier

We trained the GDA classifier and evaluated its performance with the combination the validation and test sets, with 2,684 valid and 2,152 invalid samples. To avoid overfitting, we tuned the hyperparameter  $\gamma = 0.05$  and consequently lowered the learning rate  $\alpha = 10^{-6}$ .

We use the balanced accuracy  $\bar{A} = \frac{1}{2}(A_0 + A_1)$ , where  $A_1$  and  $A_0$  are the class-wise accuracies for valid and invalid samples, respectively, and the overall accuracy  $A$  to evaluate model performance [14]. Experiments show that GDA achieves consistently high classification accuracy on the validation set, which supports our initial intuition that kernelized methods will better model the circuit response.

Indeed, we achieve  $\bar{A} \approx 0.994$ , with  $A_1 \approx 0.992$  (valid) and  $A_0 \approx 0.995$  (invalid). The overall accuracy of the model was  $A \approx 0.994$ . Since the decision boundary is in a high dimensional feature space, we visualize the boundary by plotting 2-dimensional cross sections for every pair of features. For the sake of brevity, we show four of the most interesting cross sections in Figure 3. The red and blue points represent valid and invalid combinations of these CDPs, respectively. Notice that the decision boundary well separates the two classes, as expected.

## 5.3 1-Nearest Neighbor Model Baseline

To establish a baseline for evaluating our two-stage algorithm, we implemented a straightforward 1-Nearest Neighbor (1-NN) algorithm to build a direct mapping  $1\text{-NN} : y \rightarrow x$  from desired OSCs to CDPs. From its training set, the 1-NN algorithm identifies the sample with the lowest Euclidean distance to the target OSCs, subsequently returning the associated CDPs. The 1-NN may never yield a mechanoreceptor

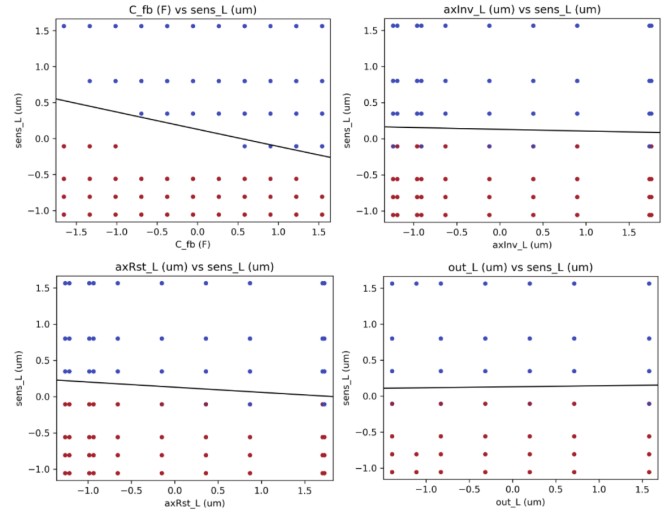


Fig. 3. GDA decision boundary cross sections

circuit that perfectly meets the target if the target is not in the dataset, and is therefore expected to be a lower bound on the performance of the two-stage pipeline.

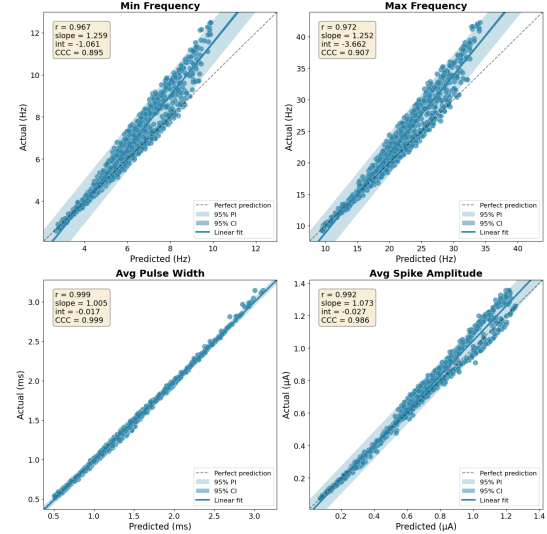


Fig. 4. Actual circuit OSCs vs. predictions from the NN.  $r$ : correlation; slope and int: slope and intercept of linear regression; CCC: concordance correlation coefficient; CI: confidence interval; PI: prediction interval.

## 5.4 Two-Stage Pipeline

For the first stage, we implement the BO algorithm given the trained NN. We defined the search bounds of the BO trust region from  $3 \mu\text{m}$  to  $35 \mu\text{m}$  to capture realistic fabrication limitations for the length parameters of the OFET technology.

For the second stage, we use the trained GDA classifier to check the CDPs proposed by the BO algorithm for validity. If the design is invalid, the BO algorithm is rerun. Note that BO is nondeterministic because of its random initialization and search procedure, so rerunning will yield different results.

For testing, we randomly generate 1,000 target OSCs  $\{y_{\text{target}}^{(j)}\}_{j=1}^{1000}$ . In order to ensure that the  $y_{\text{target}}^{(j)}$ 's are physically achievable with CDPs, we randomly sample from the distribution of valid outputs in the dataset. We also enforce a maximum duty-cycle constraint  $D_{\max} = \tau f_{\max} < 3.71\%$ . This value is chosen because 99% of valid Cadence-simulated designs in our dataset satisfy this constraint. See Appendix D for more details.

We pass these target values into the two-stage pipeline, yielding 1,000 CDPs. These CDPs are then used as input for the NN model from Stage 1 and to run the Cadence simulation. Figure 4 shows the Cadence simulation results compared to the NN predictions for each OSC. This confirms that the BO algorithm and NN model perform well overall, with near perfect matching for  $\tau$  and  $a$  compared to simulation, as their correlations are above 0.99. We get acceptable matches for  $f_{\min}$  and  $f_{\max}$ , with relatively large correlations above 0.95. This also shows that the GDA classifier is working as intended, resulting in circuits that perform as expected.

### 5.5 Model Comparison Study

We compare the baseline 1-NN model with our two-stage pipeline. To do so, we plug the same 1,000 targets as described in the previous section into the two-stage model and 1-NN. Then, we validate the proposed CDPs by simulating them in Cadence and comparing the resulting OSCs with the target OSCs.

Figure 5 further illustrates the performance of the two-stage model versus the 1-NN model in producing circuits that match the target. Across all four OSCs, the two-stage model produces predictions that more closely follow the  $y = x$  relationship. For  $\tau$  and  $a$ , the two-stage model also achieves higher CCC and narrower prediction intervals. However, for  $f_{\min}$  and  $f_{\max}$ , the two-stage model does not significantly outperform the 1-NN model in terms of correlation or prediction spread.

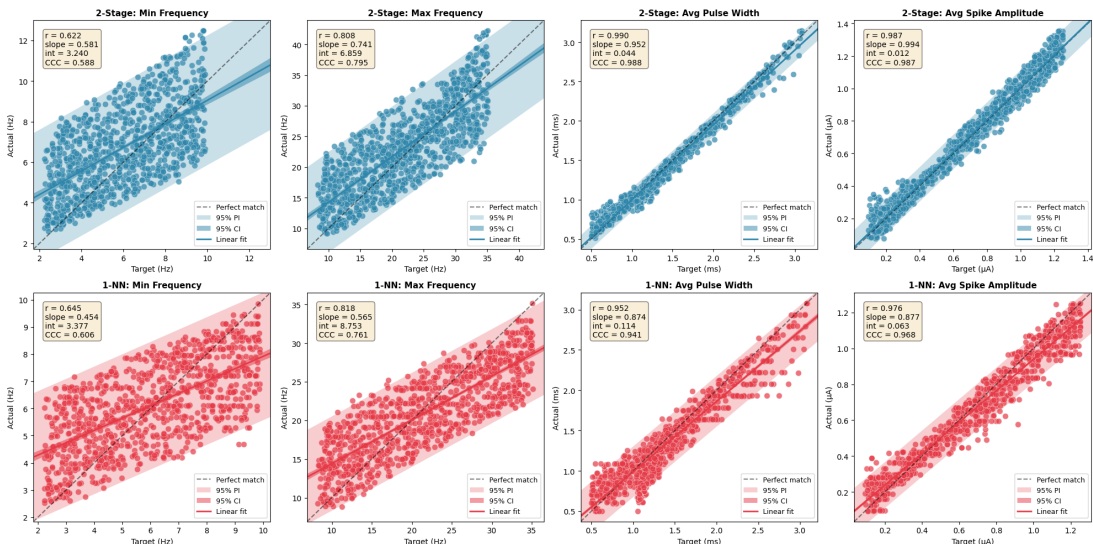


Fig. 5. Actual circuit OSCs obtained from simulation vs. target OSCs for the two-stage model and 1-NN.  $r$ : correlation; slope and int: slope and intercept of linear regression; CCC: concordance correlation coefficient; CI: confidence interval; PI: prediction interval.

## VI. CONCLUSIONS AND NEXT STEPS

The two-stage model robustly outperforms the 1-NN baseline for pulse width  $\tau$  (the most important OSC for multiplexing mechanoreceptor outputs, as explained in Appendix A) and amplitude  $a$ , confirming the validity of our inverse design approach where data coverage is sufficient. However, the persistent overprediction bias for  $f_{\min}$  and  $f_{\max}$ , despite low training losses, indicates that the current dataset fails to capture the full mapping dynamics of frequency, and is not a consequence of the models themselves. This hypothesis is supported by the poor performance of the 1-NN model in retrieving targets with matching frequency characteristics.

To improve performance, we propose three future steps:

*Fine-grained Parameter Sampling:* As noted in Appendix B, current simulations use fewer than 10 possible values for the length of OFETs. Randomly sampling values within the gaps between these points would create a more continuous dataset for fine-tuning the NN.

*Relaxing Validity Criteria:* As explained in Appendix C, currently, only the most sensitive circuits are classified as valid samples, where as only the least sensitive circuits are included as invalid samples. By accepting all circuits that produce spiking outputs at 25% compression and above as all valid and the rest as all invalid, we could fully utilize the data generated from all 23,232 CDPs rather than the current subset of 16,120.

*Reinforcement Learning (RL):* Instead of performing more parameter sweeps, as long as the compatibility issues can be resolved for a custom simulation of OFETs, we could design an RL agent that can directly interface with Cadence Spectre, as illustrated in [8]. This would allow active exploration of the design space, removing the constraints of pre-generated datasets.

## REFERENCES

- [1] Y. Nishio, D. Zhong, K. K. Kim, Q. Liu, C. Wu, J. B.-H. Tok, B. Murmann, and Z. Bao, "Intrinsically stretchable transistors and integrated circuits," vol. 2, no. 11, pp. 715–735. [Online]. Available: <https://www.nature.com/articles/s44287-025-00220-3>
- [2] D. Zhong, C. Wu, Y. Jiang, Y. Yuan, M.-g. Kim, Y. Nishio, C.-C. Shih, W. Wang, J.-C. Lai, X. Ji, T. Z. Gao, Y.-X. Wang, C. Xu, Y. Zheng, Z. Yu, H. Gong, N. Matsuhisa, C. Zhao, Y. Lei, D. Liu, S. Zhang, Y. Ochiai, S. Liu, S. Wei, J. B.-H. Tok, and Z. Bao, "High-speed and large-scale intrinsically stretchable integrated circuits," vol. 627, no. 8003, pp. 313–320. [Online]. Available: <https://www.nature.com/articles/s41586-024-07096-7>
- [3] W. Wang, Y. Jiang, D. Zhong, Z. Zhang, S. Choudhury, J.-C. Lai, H. Gong, S. Niu, X. Yan, Y. Zheng, C.-C. Shih, R. Ning, Q. Lin, D. Li, Y.-H. Kim, J. Kim, Y.-X. Wang, C. Zhao, C. Xu, X. Ji, Y. Nishio, H. Lyu, J. B.-H. Tok, and Z. Bao, "Neuromorphic sensorimotor loop embodied by monolithically integrated, low-voltage, soft e-skin," vol. 380, no. 6646, pp. 735–742. [Online]. Available: <https://www.science.org/doi/10.1126/science.ade0086>
- [4] G. Indiveri, B. Linares-Barranco, T. J. Hamilton, A. van Schaik, R. Etienne-Cummings, T. Delbrück, S.-C. Liu, P. Dudek, P. Häfliger, S. Renaud, J. Schemmel, G. Cauwenberghs, J. Arthur, K. Hynna, F. Folowosele, S. Saighi, T. Serrano-Gotarredona, J. Wijekoon, Y. Wang, and K. Boahen, "Neuromorphic silicon neuron circuits," *Frontiers in Neuroscience*, vol. 5, no. 73, pp. 1–23, 2011.
- [5] H. Wang, B. Sun, S. S. Ge, J. Su, and M. L. Jin, "On non-von Neumann flexible neuromorphic vision sensors," vol. 8, no. 1, p. 28. [Online]. Available: <https://www.nature.com/articles/s41528-024-00313-3>
- [6] Y. Zhao, J. Wang, S. Zhang, and W. Liang, "Neuromorphic olfactory perception chips: Towards universal odour recognition and cognition," vol. 2, no. 11, pp. 755–772. [Online]. Available: <https://www.nature.com/articles/s44287-025-00214-1>
- [7] K. Settaluri, A. Haj-Ali, Q. Huang, K. Hakhamaneshi, and B. Nikolic, "AutoCkt: Deep Reinforcement Learning of Analog Circuit Designs" in *2020 Design, Automation & Test in Europe Conference & Exhibition (DATE)*, pp. 490–495. [Online]. Available: <https://ieeexplore.ieee.org/document/9116200>
- [8] H. Wang, K. Wang, J. Yang, L. Shen, N. Sun, H.-S. Lee, and S. Han, "GCN-RL Circuit Designer: Transferable Transistor Sizing with Graph Neural Networks and Reinforcement Learning," in *2020 57th ACM/IEEE Design Automation Conference (DAC)*, pp. 1–6. [Online]. Available: <http://arxiv.org/abs/2005.00406>
- [9] Y. Yang, M. J. M. Hosseini, W. Kruger, and R. A. Nawrocki, "Modular modeling of analog organic neuromorphic circuits: Toward prototyping of hardware-level spiking neural networks," *IEEE Transactions on Circuits and Systems I: Regular Papers*, vol. 70, no. 3, pp. 1161–1174, 2022.
- [10] L. Shao, T.-C. Huang, T. Lei, Z. Bao, R. G. Beausoleil, and K.-T. Cheng, "Compact modeling of carbon nanotube thin-film transistors for flexible circuit design," *IEEE Transactions on Electron Devices*, vol. 65, no. 10, pp. 4136–4142, 2018.
- [11] Z. Xu, H. Wang, J. M. Phillips, and S. Zhe, "Standard gaussian process can be excellent for high-dimensional bayesian optimization," *arXiv preprint arXiv:2402.02746*, 2024.
- [12] J. Santiago, M. Claeys-Bruno, and M. Sergent, "Construction of space-filling designs using wsp algorithm for high dimensional spaces," in *Chemometrics and Intelligent Laboratory Systems*, 2011.
- [13] I. Goodfellow, Y. Bengio, and A. Courville, *Deep Learning*. MIT Press, 2016. [Online]. Available: <https://www.deeplearningbook.org>
- [14] A. Ng and T. Ma, *CS229 Lecture Notes*, Online lecture notes, 2023, [https://cs229.stanford.edu/notes2022fall/main\\_notes.pdf](https://cs229.stanford.edu/notes2022fall/main_notes.pdf).
- [15] S. C. B. Mannsfeld, B. C.-K. Tee, R. M. Stoltberg, C. V. H.-H. Chen, S. Barman, B. V. O. Muir, A. N. Sokolov, C. Reese, and Z. Bao, "Highly sensitive flexible pressure sensors with microstructured rubber dielectric layers," vol. 9, no. 10, pp. 859–864. [Online]. Available: <https://www.nature.com/articles/nmat2834>

## TEAM CONTRIBUTIONS

- **Luke Qiao:** Implemented GDA for supervised classification of valid and invalid CDP combinations. Help with generating organic IC dataset. Implemented the BO

algorithm and two-stage model. Worked on report, poster and presentation.

- **Xingyu (Brian) Zhou:** Designed the neuromorphic mechanoreceptor circuit. Performed high-throughput parallelized circuit simulations, and compiled the simulation results into data for training. Implemented the 1-NN model. Provided design feedbacks to the BO algorithm, ensuring it is physically relevant. Analyzed experiment results. Worked on report, poster and presentation.
- **Adhavan Jayabalan:** Implemented unsupervised classification algorithms to cluster data for analysis. Built and trained the NN model. Helped with preprocessing the dataset. Worked on report, poster and presentation.

## APPENDIX A

### *Mechanoreceptor Circuit Mechanism of Operation*

The schematic of the mechanoreceptor circuit is shown in Figure 6. The pressure sensing OFET  $M_{\text{sens}}$  has special gate dielectric material such that the gate channel capacitance would be proportional to the pressure applied to the gate. Therefore, its drain current  $I_{DS}$  reflects the magnitude of the applied pressure.  $M_0$  to  $M_3$  is a cascaded current mirror that not only relays the  $I_{DS}$  of  $M_{\text{sens}}$  to the axon hillock but also ensures high output impedance for good isolation of  $M_{\text{sens}}$ .

In the axon hillock, the membrane capacitance  $C_{\text{mem}}$  accumulates the current from  $M_{\text{sens}}$ . As the voltage across the membrane capacitor, the membrane voltage  $V_{\text{mem}}$ , crosses the inversion threshold of the CMOS inverter  $M_4$  to  $M_5$ ,  $V_{\text{out}}$  is driven close to supply voltage  $V_{DD}$  because the output from  $M_4$  to  $M_5$  is once more inverted by  $M_6$  to  $M_7$ . While  $V_{\text{out}}$  is close to  $V_{DD}$ ,  $M_{\text{rst}}$  is turned on to pull  $V_{\text{mem}}$  back to ground, which in turn pulls  $V_{\text{out}}$  close to ground, forming a spike. The feedback capacitor  $C_{\text{fb}}$  moderates the rate at which  $V_{\text{mem}}$  and  $V_{\text{out}}$  changes since the voltage across a capacitor cannot be changed instantaneously.

An example of the traces of  $V_{\text{mem}}$  and  $V_{\text{out}}$  of two mechanoreceptor circuits is shown in Figure 7. The CDPs of these two circuits are chosen so that for the same level of applied pressure, their output frequencies are similar but their pulse widths are different. In this way, when the  $V_{\text{out}}$  traces are converted to current by  $M_{\text{out}}$  and then summed together through Kirchhoff's Current Law, the two frequency components will still be clearly distinguishable.

## APPENDIX B

### *Parameter Values for Simulation*

The values for each parameter are primarily chosen from measurements obtained from real stretchable OFETs, fabricated in a batch from May 2025. Specifically,  $C_{\text{sens}}$  has a baseline value of  $17.67 \text{ nF/cm}^2$ , whereas OFET lengths ( $\text{axInv\_L}$ ,  $\text{axRst\_L}$ ,  $\text{out\_L}$ ,  $\text{sens\_L}$ ) may take a value of approximately  $4 \mu\text{m}$ ,  $7 \mu\text{m}$ , or  $33 \mu\text{m}$ . The widths of the OFETs are all fixed at about  $175 \mu\text{m}$ . In order to gather more data, we also included OFET lengths of  $10 \mu\text{m}$ ,  $15 \mu\text{m}$ ,  $20 \mu\text{m}$  and  $25 \mu\text{m}$ . These values, though not coming from real OFET measurements, should be attainable as the process

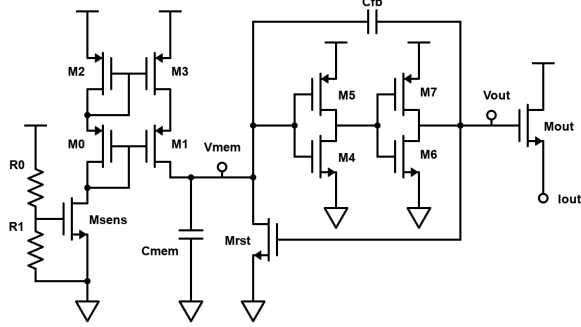


Fig. 6. Schematic of the Mechanoreceptor Circuit

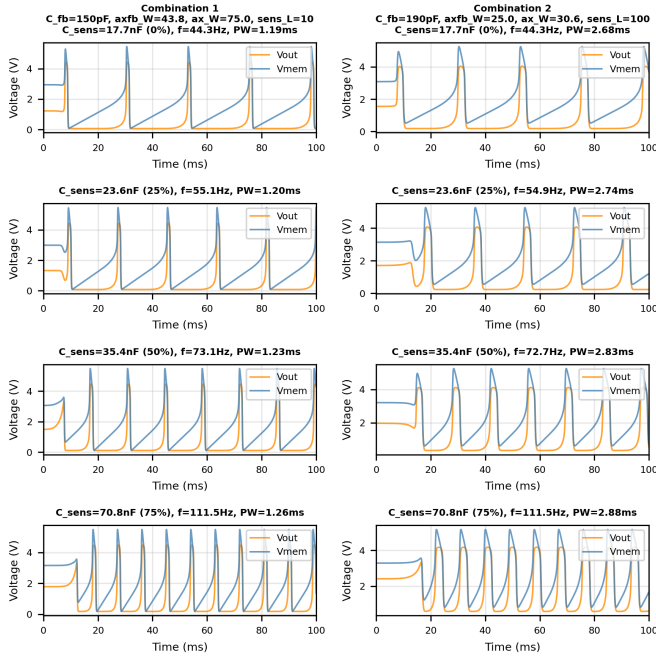


Fig. 7.  $V_{\text{out}}$  and  $V_{\text{mem}}$  of Two Distinct Mechanoreceptor Circuits Across 4 Levels of Applied Pressure

technology can achieve OFET lengths as low as  $4 \mu\text{m}$  and as high as  $33 \mu\text{m}$ . For feedback capacitor  $C_{\text{fb}}$ , it is swept across 100 pF to 200 pF at 10 pF intervals.

To simulate applied pressure, by Hooke's Law, it is assumed that the change in applied pressure is linearly proportional to the change in thickness of the gate capacitance of  $M_{\text{sens}}$ . If we further assume that the gate capacitance of  $M_{\text{sens}}$  can be treated as a parallel plate capacitor  $C = \frac{\epsilon A}{d}$ , then the change in the inverse of its capacitance would be linearly proportional to the change in its thickness. Consequently, we simulate 4 levels of pressure respectively causing minimal gate thickness compression, 25% gate thickness compression, 50% gate thickness compression and 75% gate thickness compression, by choosing  $C_{\text{sens}} = 17.67/(1 - 0\%)$ ,  $17.67/(1 - 25\%)$ ,  $17.67/(1 - 50\%)$ ,  $17.67/(1 - 75\%)$  nF/cm<sup>2</sup>.

It must be noted that  $M_{\text{sens}}$  is simulated as a regular n-type OFET in the simulation, as a sensing OFET fabricated with the latest intrinsically stretchable process technology does not exist yet. Therefore, the quantitative assumptions made on the relationship between applied pressure and  $C_{\text{sens}}$  may not apply. However, qualitatively a positive correlation between applied pressure and  $C_{\text{sens}}$  was confirmed in sensing OFETs fabricated with a much older process technology [15].

## APPENDIX C

### Validity vs. Invalidity Criteria

In the simulation data, it is mostly observed that "invalid" CDP combinations yield mechanoreceptor circuits that do not produce spiking  $I_{\text{out}}$  until the gate thickness compression reaches a certain level. e.g. flat line output for minimal and 25% gate thickness compression, but spiking output for 25% and 75% compression. These circuits are still technically functional, but may have an activation threshold too high to be useful for the electronic skin. Considering this observation as well as the goal to obtain the most sensitive mechanoreceptor circuit designs, only invalid samples that do not produce spikes until 75% compression are included in the dataset.

## APPENDIX D

### Feasibility of Targets

The distribution of valid and invalid targets is shown in Figure 8. We get that 99% of dataset points lie below the boundary  $\tau f_{\max} = 3.71\%$  indicating that this cutoff accurately captures the region of feasible targets that are able to be realized by some combination of CDPs.

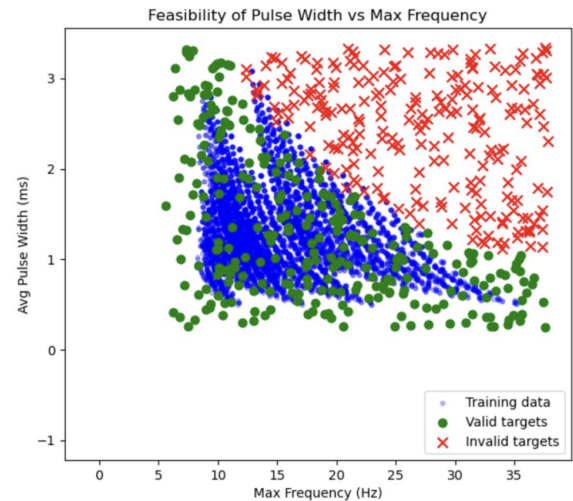


Fig. 8. Target Feasibility Distribution